



https://doi.org/10.1016/j.ultrasmedbio.2021.11.010

Original Contribution

VERY LOW FREQUENCY RADIAL MODULATION FOR DEEP PENETRATION CONTRAST-ENHANCED ULTRASOUND IMAGING

BOWEN JING, A and BROOKS D. LINDSEY A,B

^a Wallace H. Coulter Department of Biomedical Engineering, Georgia Institute of Technology and Emory University, Atlanta, Georgia, USA; and ^b School of Electrical and Computer Engineering, Georgia Institute of Technology, Atlanta, Georgia, USA

(Received 16 May 2021; revised 16 November 2021; in final form 21 November 2021)

Abstract—Contrast-enhanced ultrasound imaging allows vascular imaging in a variety of diseases. Radial modulation imaging is a contrast agent-specific imaging approach for improving microbubble detection at high imaging frequencies (>7.5 MHz), with imaging depth limited to a few centimeters. To provide high-sensitivity contrast-enhanced ultrasound imaging at high penetration depths, a new radial modulation imaging strategy using a very low frequency (100 kHz) ultrasound modulation wave in combination with imaging pulses <5 MHz is proposed. Microbubbles driven at 100 kHz were imaged in 10 successive oscillation states by manipulating the pulse repetition frequency to unlock the frame rate from the number of oscillation states. Tissue background was suppressed using frequency domain radial modulation imaging (F-RMI) and singular value decomposition-based radial modulation imaging (S-RMI). One hundred-kilohertz modulation resulted in significantly higher microbubble signal magnitude (63-88 dB) at the modulation frequency relative to that without 100-kHz modulation (51-59 dB). F-RMI produced images with high contrast-to-tissue ratios (CTRs) of 15 to 22 dB in a stationary tissue phantom, while S-RMI further improved the CTR (19-26 dB). These CTR values were significantly higher than that of amplitude modulation pulse inversion images (11.9 dB). In the presence of tissue motion (1 and 10 mm/s), S-RMI produced high-contrast images with CTR up to 18 dB; however, F-RMI resulted in minimal contrast enhancement in the presence of tissue motion. Finally, in transcranial ultrasound imaging studies through a highly attenuating ex vivo cranial bone, CTR values with S-RMI were as high as 23 dB. The proposed technique demonstrates successful modulation of microbubble response at 100 kHz for the first time. The presented S-RMI low-frequency radial modulation imaging strategy represents the first demonstration of real-time (20 frames/s), high-penetration-depth radial modulation imaging for contrast-enhanced ultrasound imaging. © 2021 World Federation for Ultrasound in Medicine & Biology. All rights reserved.

Key Words: Contrast agent, Low-frequency ultrasound, Radial modulation, Transcranial ultrasound.

INTRODUCTION

Contrast-enhanced ultrasound (CEUS) imaging with microbubble contrast agents enables low-cost, safe visualization and quantification of local perfusion dynamics in a variety of diseases affecting vasculature, including cancer and cardiovascular disease (Averkiou et al. 2020; Erlichman et al. 2020). Various CEUS imaging techniques have been proposed for mapping local hemodynamics, including parametric perfusion imaging and microvascular imaging (Strobel et al. 2008; Jang et al. 2009; Dietrich et al. 2012; Lin et al. 2017; Lindsey et al. 2017a, 2017b), with a preference for using high frequencies to provide high spatial resolution. In applications requiring

Correspondence to: Biomedical Engineering, Georgia Institute of Technology and Emory University, 2107 Whitaker Building, 313 Ferst Drive, Atlanta, GA 30332.

deeper penetration, such as guiding biopsy in hepatic masses (Wu et al. 2006; Yoon et al. 2010) and transcranial ultrasound imaging in stroke (Seidel et al. 2003, 2013; Kern et al. 2011), CEUS is a useful diagnostic imaging tool; however, sensitivity can be limited in these cases of high attenuation and penetration depth.

In imaging abdominal organs including the liver, pancreas, spleen and kidney, low transmit frequencies (2–5 MHz) (American Institute of Ultrasound in Medicine [AIUM] 2012) are usually required to achieve sufficient penetration, especially for individuals with high body mass index (~35% of cases) (Lyshchik et al. 2018; Putz et al. 2019). For transcranial CEUS, transmit frequencies ranging from 1 to 3 MHz are usually used to ensure sufficient imaging depth and signal-to-noise ratio, even when imaging through the temporal bone window (Lindsey et al. 2014a, 2014b;

Vinke et al. 2017; Jing et al. 2020a, 2020b). While nonlinear multipulse CEUS techniques at 2 to 5 MHz (Phillips 2001; Eckersley et al. 2005; Whittingham 2005; Kusunose and Caskey 2018) have been widely used for imaging deep regions in scenarios such as abdominal (Strobel et al. 2008; Sidhu et al. 2018) and transcranial (Vinke et al. 2017) imaging, tissue signal decorrelation caused by physiological motion and non-linear propagation results in significant tissue artifacts and degrades the contrast-to-tissue ratio (CTR) (Krishnan et al. 1998; Zhao et al. 2007; Couture et al. 2008; Tang et al. 2010; Stanziola et al. 2019; Averkiou et al. 2020). Subharmonic imaging provides improved imaging depth by detecting signals arising from microbubbles at frequencies one-half transmitted equal the frequency (Shi al. 1999: Forsberg et al. 2006: Eisenbrey et al. 2011); however, it is challenging to suppress the reflections from the highly heterogeneous tissues (Eisenbrey et al. 2011). Multiple plane wave imaging with coded pulses has also improved the CTR for deep CEUS imaging (Gong et al. 2018; Shen and Yan 2019). In addition, superharmonic imaging transmits low-frequency ultrasound near the microbubble resonance frequency and forms images using superharmonics produced only by the microbubbles (Bouakaz et al. 2002a, 2002b, 2003; Kruse and Ferrara 2005; Guiroy et al. 2013); however, the penetration depth is limited because of the high frequencies of signals produced by microbubbles (Lindsey et al. 2014a, 2014b, 2015). As an alternative to imaging the non-linearity of microbubbles, ultrafast imaging relies on the low spatial coherence of flowing agents to image the vascular network. This technique is promising, but separating tissue from microbubbles is challenging in cases of slow flow or fast physiological motion (Errico et al. 2015; Muleki-Seya et al. 2019).

Radial modulation imaging represents an alternative in which low-frequency ultrasound waves are used to modulate the size and thus the high-frequency scattering characteristics of microbubbles (Bouakaz et al. 2007; Chérin et al. 2008; Masoy et al. Phillips et al. 2008; Emmer et al. 2009; Hansen and Angelsen 2009; Cheng et al. 2011; Renaud et al. 2014; Yu et al. 2014; Muleki-Seya et al. 2019). This imaging approach does not rely on the flow of microbubbles or on harmonics and thus is suitable for vascular imaging at high penetration depths and in the presence of relatively slow blood flow or fast physiological motion. However, as indicated by previous studies (Shariff et al. 2006; Chérin et al. 2008), a large separation between the modulation and imaging frequencies is typically needed to avoid artifacts arising from the coupling of the harmonics of the low-frequency modulation wave. As the modulation frequency used in these studies was at least 0.5 MHz, images were mostly acquired using a high imaging frequency (≥7.5 MHz) (Shariff et al. 2006; Masoy et al. 2008; Phillips et al. 2008; Yu et al. 2014; Muleki-Seya et al. 2019), which limited application of radial modulation strategies for imaging deeper into tissue.

To improve imaging depth for applications such as abdominal and transcranial imaging, we propose a strategy in which very low frequency ultrasound (100 kHz) is used to modulate microbubble oscillation; then images are acquired at frequencies typically used in diagnostic ultrasound imaging (<5 MHz). While decreasing the frequency of both the modulation pulse and the imaging pulse maintains the separation required to avoid harmonic artifacts, this approach encounters the alternative challenge of providing sufficient image contrast at modulation frequencies significantly below microbubble resonance. We also propose unlocking the frame rate from the number of microbubble oscillation states for the first time by manipulating the pulse repetition frequency to retain a large number of transmit events without compromising imaging frame rate or depth. This is important to avoid high microbubble decorrelation when the blood flow rate is too high—or when the frame rate is too low-which may cause a decrease in CTR (Muleki-Seya et al. 2019).

This article is structured as follows. First, microbubble oscillation caused by a low-frequency modulation pulse is simulated. Next, the low-frequency radial modulation imaging sequence is described. The feasibility of the proposed low-frequency radial modulation imaging technique for deep-penetration, high-contrast imaging is then evaluated in tissue-mimicking phantoms. including in the presence of tissue motion, which is common in abdominal imaging because of respiration. To form CEUS images in the presence of varying degrees of physiological motion, both a frequency domain processing method and a singular value decomposition (SVD) method have been adopted, and their performance is compared. Finally, in the last part of this study, the performance of this imaging technique is tested in a highly attenuating scenario, transcranial ultrasound imaging.

METHODS

Numerical simulation of low-frequency excitation of microbubbles

To assess the feasibility of the very low frequency radial modulation contrast-enhanced imaging approach, numerical simulations of microbubble oscillation were performed. The model of Morgan et al. (2000) was used to simulate the oscillation of a 1.2- μ m-diameter microbubble using the proposed very low frequency radial modulation strategy in which microbubbles driven at 100 kHz were imaged in 10 successive oscillation states (described in greater detail in the next section). The

physical properties of the microbubble in simulations were in accordance with previous characterization of the commercial lipid-shelled microbubble (Tu et al. 2011), which is similar to the microbubble used in this study. The sequence comprised a short 2cycle, 5-MHz imaging pulse with an amplitude of 74 kPa and a 10-cycle, 100-kHz modulation pulse with an amplitude of 16 kPa. Three sets of simulations were obtained by transmitting the 5-MHz pulse at different phases relative to the 100-kHz wave: (i) with the 5-MHz pulse at the negative peak, (ii) at the positive peak and (iii) in the equilibrium phase. The scattered ultrasound wave was recorded at a distance of 50 mm from the microbubble.

Very low frequency radial modulation imaging sequence

In experimental studies, a low-frequency ultrasound transducer (BQLZR, Beijing, China) was driven at a frequency of 100 kHz using a waveform generator (AFG3021C, Tektronix, Beaverton, OR, USA) and power amplifier (2200L, E&I, Rochester, NY, USA) to provide the very low frequency modulation pulse. The diameter of the transducer is 45 mm. While previous studies on ultrafast radial modulation imaging have used a bandpass filter to extract bubble signals to form highcontrast images, the microbubble decorrelation arising when the flow rate is too high relative to the frame rate may decrease the CTR (Muleki-Seya et al. 2019). A high frame rate avoids decrease in the CTR; however, the frame rate of ultrafast acquisition is constrained by both the number of transmits per frame (i.e., for coherent plane wave compounding) and the detection states of oscillating microbubbles. While previous studies with high-frame-rate radial modulation indicate that at least three detection states during each oscillation cycle are needed to provide sufficient contrast (Muleki-Seya et al. 2019), maintaining a high frame rate requires a high pulse repetition frequency (PRF) and a limited number of transmits per frame, which is sufficient only for imaging shallow targets (Muleki-Seya et al. 2019). For imaging deeper targets, a greater number of transmit events would be required to retain the signal-to-noise ratio (SNR). Therefore, to retain a large number of transmit events without compromising high imaging frame rate, we propose unlocking the frame rate constraint from the microbubble oscillation state by manipulating the pulse repetition frequency, which is described in greater detail below.

A programmable ultrasound scanner (Vantage 256, Verasonics, Kirkland, WA, USA) was used to image microbubbles at a frequency ≤5 MHz. To improve the SNR, five successive plane wave transmits were used in each frame to acquire five sets of beamformed in-phase quadrature (IQ) data. The IQ data were then formed into

an image of microbubbles at a specific oscillation state. To ensure that the modulated microbubbles at each point in the field of view were imaged at the same phase across five plane wave transmits, no steered (tilted) transmit events were used in this study. Importantly, imaging pulses were transmitted at varying pulse repetition intervals. Specifically, for the first through fourth transmit/ acquisition events, the interval between each subsequent event was 200 μ s, and the time delay between the fifth transmit event and the start of the next frame was 201 μ s (Fig. 1a). As the microbubble was modulated at a frequency of 100 kHz, non-tilted plane wave transmits with $200-\mu s$ intervals ensured the microbubbles were sampled at the same state of the oscillation across five transmit/ acquisition events. With the additional 1- μ s delay between frames, the microbubbles driven at 100 kHz were imaged at 10 successive oscillation states (Fig. 1a) for every 10 successive images. The final imaging frame rate was approximately 1000 frames/s (i.e., $1/[5 \times 200]$ μs]). On the basis of previous studies (Muleki-Seya et al. 2019), imaging contrast increases when the number of states increases, which could be because using more microbubble modulation states provided more information. However, the maximum number of imaging states that can be achieved in our study is 10 because the resolution of the time delay between frames is 1 μ s for our system (Verasonics). As the echogenicity of tissue is assumed to be independent of the 100-kHz ultrasound wave, the resulting image will only exhibit variation in the echogenicity of microbubbles caused by the 100-kHz modulation wave.

In this study, two different processing strategies were used to isolate the microbubble signal from the tissue signal and generate the radial modulation images from the data acquired using the described sequence. The first processing method was implemented in the frequency domain and applied to the beamformed data in the slow time direction. The received IQ data were coherently summed, and a fast Fourier transform was implemented along the slow time direction for each pixel in the image. Then the mean amplitude of the signal within the frequency band centered at a normalized modulation frequency of 0.1 (from 0.08 to 0.12) was calculated at each pixel to form the final radial modulation image. It should be noted that the method is implemented efficiently in the frequency domain rather than using time-domain bandpass filtering, which is different from the method used in a previous study of high-frame-rate radial modulation imaging (Muleki-Seya et al. 2019). Images obtained using the frequency domain radial modulation imaging approach are denoted as F-RMI.

The second processing method is based on singular value decomposition (SVD) filtering (Demené et al. 2015) and was applied to the same data acquired

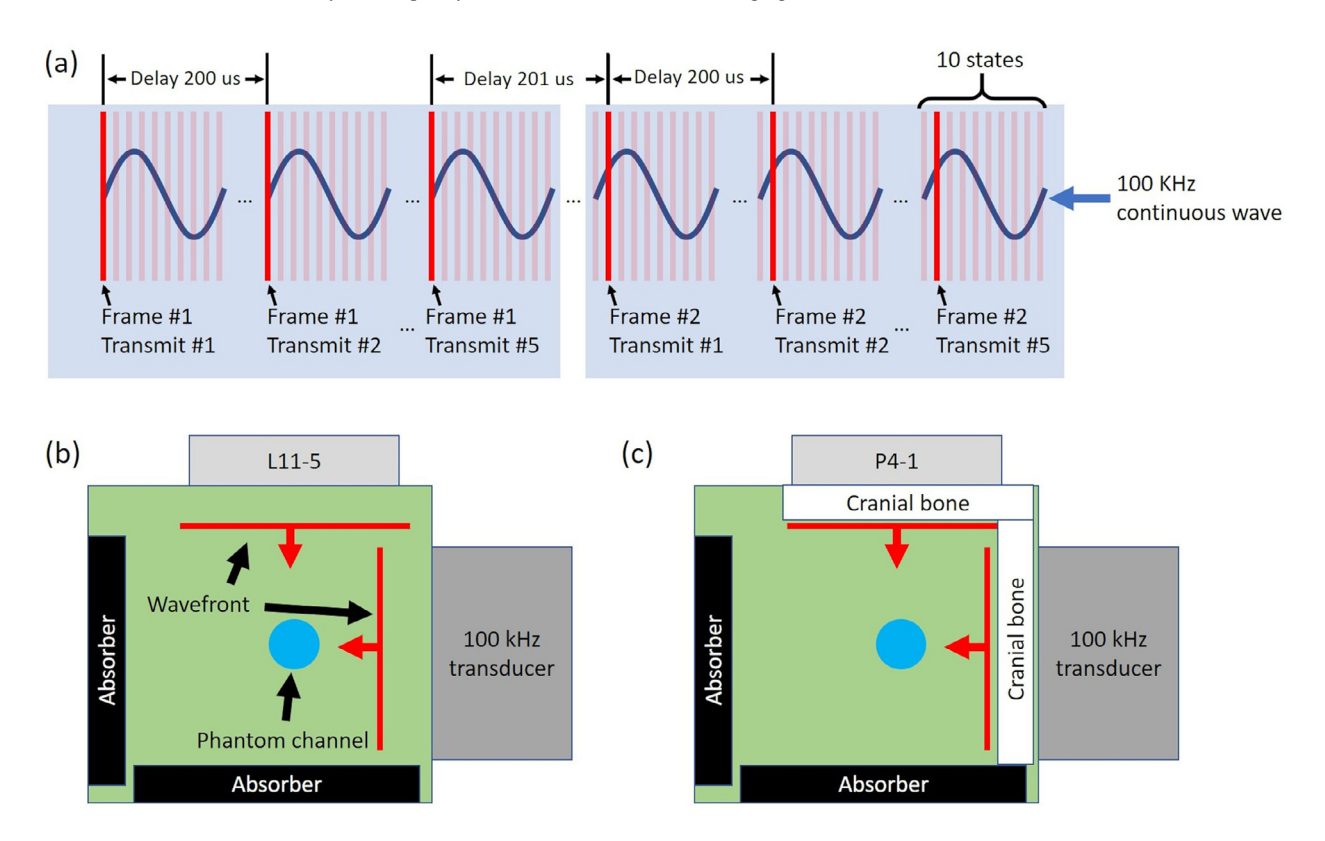


Fig. 1. Imaging sequence (a) and experimental setups for (b) 100 kHz + 5 MHz imaging experiment and (c) 100 kHz + 2 MHz transcranial imaging experiment.

using the described sequence. The five received sets of IQ data, corresponding to five successive plane wave acquisitions, were each filtered using an SVD filter to suppress the tissue background signal. It should be noted that each of the five sets contained 50 frames in this study, which means that the input of the SVD filter was 50 frames. Next, the filtered five sets of IQ data were separated into two different groups—one containing acquisitions 1, 3 and 5, and the other containing acquisitions 2 and 4—and coherently summed within each group. The final image was obtained by calculating the square root of the correlation between the two groups of data. Images obtained using the SVD filtering radial modulation imaging approach are denoted as S-RMI. This correlation-based processing method has exhibited high contrast in Doppler imaging (Huang et al. 2021) and represents an alternative to the lock-in amplifier approach used for ultrafast radial modulation imaging (Muleki-Seya et al. 2019). Fifty frames of images were used for both F-RMI and S-RMI processing in this study.

Contrast agents and tissue-mimicking phantom

The microbubbles used in the present study were synthesized in-house according to the protocol previously described (Shelton et al. 2016; Lindsey et al. 2017b). Lipid solution was prepared using

a 9:1 molar ratio of 1,2-distearoyl-sn-glycero-3-phosphocholine (DSPC) and 1,2-distearoyl-sn-glycero-3-phosphoethanolamine-N-methoxy(polyethylene glycol)-2000 (DSPE-PEG2000) (Avanti Polar Lipids, Alabaster, AL, USA) in a solution containing propylene glycol 15% (v/v), glycerol 5% (v/v) and phosphate-buffered saline (PBS) 80% (v/v). After degassing of the lipid solution in 3-mL glass vials, the headspace of the vial was filled with octafluoropropane gas. Microbubbles were formed by agitation using a Vialmix device (Lantheus Medical Imaging, North Billerica, MA, USA). The microbubble concentration, which was obtained using a Multisizer 4 equipped with a 20- μ m aperture, was 4.8 $\times 10^8$ microbubbles/mL. The mode size of the microbubble based on volume concentration was 1.2 μ m.

A tissue-mimicking phantom was fabricated using gelatin (0.06 g/mL), glutaraldehyde (1.2% v/v) and water (93.8% v/v). Graphite powder (0.06 g/mL) was added to the phantom to produce acoustic scattering. The attenuation coefficient of the phantom was approximately 2.8 dB/cm at 5 MHz.

Experimental setup

Feasibility of very low frequency radial modulation imaging. To determine the feasibility of modulating and detecting microbubbles using the proposed strategy with a 100-kHz wave and an imaging pulse in the low-megahertz range, an experiment was performed with the 100-kHz transducer placed outside of a plastic container (Fig. 1b). This container was filled with microbubbles diluted by a factor of 30,000 (1.6 × 10⁴ microbubbles/mL). A linear array transducer (L11-5, ATL, Bothell, WA, USA) was placed above the phantom. One-cycle, 5-MHz pulses were transmitted for imaging. Ultrasound images were not saved until the motion of microbubbles was minimal, although not fully stationary. One hundred fifty frames of compounded images were acquired at approximately 1000 frames/s in the presence of 100-kHz continuous wave modulation.

Next, the imaging performance of the 100 kHz + 5 MHz imaging strategy was evaluated in a tissue-mimicking phantom with a 4-mm-diameter channel. The microbubbles from the vial were diluted by a factor of 20,000 (2.4 \times 10⁴ microbubbles/mL) and infused into the phantom channel. The acoustic pressure of the imaging pulse was 74 kPa at a depth of 20 mm. In addition to the case without using 100-kHz ultrasound, five different voltage levels were used to drive the 100-kHz transducer for modulation during imaging. A low-frequency hydrophone (TC 4038, RESON, Camarillo, CA, USA) with a linear receiving response from 100 to 500 kHz was used to measure the acoustic output of the 100-kHz transducer at different acoustic levels. To prevent any damage to the hydrophone, the highest two pressure levels were obtained by linearly extrapolating the low acoustic measurements. Based on the acoustic measurements and attenuation of the phantom, the negative acoustic pressures of the 100-kHz wave were estimated to be 8, 16, 30, 61 and 121 kPa.

An ensemble of 50 frames was acquired, which would allow real-time imaging at approximately 20 frames/s. For each pressure level, five sets of data were acquired. To simulate the slowest moving microbubbles perfusing capillaries, there was a 30-s pause after the infusion was stopped to minimize the motion of microbubbles in the phantom channel before each data acquisition. To produce S-RMI images, the first, largest singular value was discarded to filter out tissue background.

As indicated in previous studies, radial modulation image quality degrades because of the presence of artifacts when the high-frequency signal is generated by microbubbles excited at low frequency and coupled into the bandwidth of the imaging transducer (Chérin et al. 2008). These high-frequency artifacts, which could be harmonics or broadband signal generated from either stable or inertial cavitation, should be avoided. In this study, to isolate and monitor the high-frequency artifacts generated by 100-kHz ultrasound, five sets of ultrasound data were acquired for each low-frequency ultrasound pressure level without transmission

of 5-MHz imaging pulses. The average signal magnitude of all pixels in the field of view was obtained. The receiving bandwidth was from approximately 4 to 10 MHz. In addition, to analyze the cavitation at each pressure level of 100-kHz ultrasound, a 5-MHz singleelement piston transducer (V309, Panametrics, Waltham, MA, USA) was used to passively receive acoustic signals for 4 ms at a sampling frequency of 100 MHz (PDA14, Signatec, Newport Beach, CA, USA). The acquisition was repeated 20 times at each pressure level. The power spectrum was obtained using fast Fourier transform. As the duration of the passive acquisition (4 ms) was much longer than the acquisition obtained by the Verasonics system, the frequency resolution (250 Hz) was sufficient to identify the harmonics (e.g., 200 kHz) and ultraharmonics (e.g., 150 kHz) of microbubbles modulated at 100 kHz.

In addition, the described RMI approaches were also compared with a non-linear microbubble-specific imaging technique, amplitude modulation pulse inversion (AMPI) (Phillips 2001; Eckersley et al. 2005). AMPI is a widely used contrast pulse sequence (CPS) (Phillips 2001, Whittingham 2005). AMPI provides higher CTRs than the pulse inversion (PI) because of the additional modulation of the pulse amplitude. Seventeen steered transmit events at varying angles $(-10^{\circ} \text{ to } 10^{\circ})$ were used to produce each frame for AMPI imaging, as in previous studies (Jing et al. 2020a, 2020b). Three 4.5-MHz pulses (one full-amplitude pulse and two inverted half-amplitude pulses) were transmitted at each angle. The two half-amplitude pulses were transmitted using only even or odd elements, respectively. The received radiofrequency data sampled at 31.25 MHz were summed for each angle before being reconstructed into beamformed IQ data. Before data acquisition, the transmit amplitude was optimized to produce the highest contrast while avoiding microbubble destruction. The in situ pressure of the full-amplitude transmitted pulse was estimated to be 41 kPa based on acoustic measurements and phantom attenuation.

Evaluation of very low frequency radial modulation imaging performance in the presence of motion. Physiological tissue motion, such as respiratory motion, may induce a Doppler shift in slow time and result in prominent tissue artifacts in contrast-specific imaging techniques. Therefore, the performance of the proposed low-frequency radial modulation imaging strategy in the presence of motion was also assessed. Respiratory motion is often seen when imaging abdominal tissues such as the liver and kidney (Averkiou et al. 2010; Mule et al. 2011; Wang et al. 2019); thus, motion similar to respiratory motion was induced at high and low velocities (1 and 10 mm/s) (Seppenwoolde et al. 2002) by attaching the transducer to a computer-controlled motion

stage (XPS-Q8, Newport, Irvine, CA, USA). The motion was in the axial direction (*i.e.*, along the beam). Both F-RMI and S-RMI processing approaches were applied to the acquired imaging data, and resulting CTR values were compared. The total displacement of the transducer array during imaging was approximately 0.05 mm at 1 mm/s and 0.5 mm at 10 mm/s. The F-RMI image was obtained using the frequency domain processing method described above, while S-RMI images described in the Results represent the optimal singular value cutoff yielding the maximum CTR for each data set.

Transcranial imaging

In addition to imaging in the presence of physiological motion, imaging at high penetration depths or high attenuation is also a challenge for contrast-enhanced ultrasound, with transcranial assessment of brain perfusion through the intact adult cranial bone representing a particularly challenging application. To test imaging performance in this highly attenuating scenario, a custom transcranial imaging phantom was designed, as illustrated in Figure 1c. To achieve better penetration for this application, a P4-1 transducer array (ATL) was used to transmit imaging pulses at 2 MHz. An ex vivo human temporal bone with a thickness of approximately 3 mm was placed between the P4-1 array and the phantom. A 6-mm-thick ex vivo parietal bone was placed between the 100-kHz transducer and the phantom. Images were processed using the S-RMI technique, with the largest singular value being discarded to suppress the signal of the tissue background. All skull samples used in this work were purchased from Skulls Unlimited International Inc. (Oklahoma City, OK, USA), a supplier of skulls for researchers; thus, no identifying information was collected and no institutional review board (IRB) approval was required. Transcranial AMPI images were also acquired. Images were obtained using steered transmit events at 17 angles $(-10^{\circ} \text{ to } 10^{\circ})$. At each angle, three one-cycle pulses (one full-amplitude pulse and two inverted half-amplitude pulses) at a center frequency of 1.5 MHz were transmitted using a P4-1 array.

Statistical analysis

To quantify the performance of this microbubble-specific imaging method, the CTR was quantified according to the equation $CTR = 20 \times \log_{10} (S_{Microbubble}/S_{Tissue})$. $S_{Microbubble}$ is the mean signal magnitude of microbubbles, and S_{Tissue} is the signal magnitude of the tissue-mimicking phantom background. CTR has been widely used in previous studies of contrast-enhanced ultrasound imaging techniques (Desailly et al. 2017; Gong et al. 2018). As off-axis artifacts are present at the same depth as the microbubbles because of unfocused transmit events, during CTR quantification, we measured

the tissue signal at locations that were slightly different from the depth of microbubbles to minimize the bias of the measurement. To compensate for variation in signal magnitude caused by the attenuation and variation of the receiving beamforming aperture, we intentionally measured the tissue signal at both shallower and deeper locations relative to the region of microbubbles and averaged these measurements. In this study, five independent sets of data were acquired for each condition and each imaging technique. The differences in decibel-scaled signal magnitude and CTR between different pressure levels were tested using a non-parametric method, the Kruskal-Wallis test. The comparison between two cases among multiple cases was carried out using Tukey's honestly significant difference procedure. The difference between two different processing methods, F-RMI and S-RMI, was tested using the Mann–Whitney *U*-test. The difference was considered significant when the p value was less than 0.05.

RESULTS

Numerical simulations

The 100 kHz + 5 MHz transmits (Fig. 2a) induced high-frequency oscillation superimposed on the 100-kHz oscillation (Fig. 2b). The scattered wave is illustrated in Figure 2c for the three simulated conditions in Figure 2a. Specifically, the positive amplitude of the scattered 5-MHz wave reached the maximum value (6.31 Pa) when the 5-MHz pulse was transmitted at the positive pressure peak of the 100-kHz wave. The lowest amplitude (5.04) Pa) of the scattered wave was seen when the 5-MHz pulse was transmitted at the negative pressure peak of the 100-kHz wave. Overall, the peak negative amplitude of the scattered high-frequency wave was modulated by the 100 kHz wave when the high-frequency pulse was transmitted at different phases of the 100-kHz ultrasound. This variation in microbubble response and scattered pressure waves suggests that 100-kHz modulation may be feasible for imaging.

Ultrasound detection of radially modulated microbubbles

Figure 3a is an image of microbubbles in water with 100-kHz modulation. After the low-frequency component in the IQ data along the slow time direction is filtered out, multiple angled stripes can be seen in the images (Fig. 3b), illustrating the signal magnitude of the microbubbles varying sinusoidally (Fig. 3c). The power spectrum (Fig. 3d) of the signal in slow time exhibits a peak at a normalized frequency of 0.1, which indicates that the microbubbles can be modulated and the resulting signal can be detected using the 100 kHz + 5 MHz radial modulation technique.

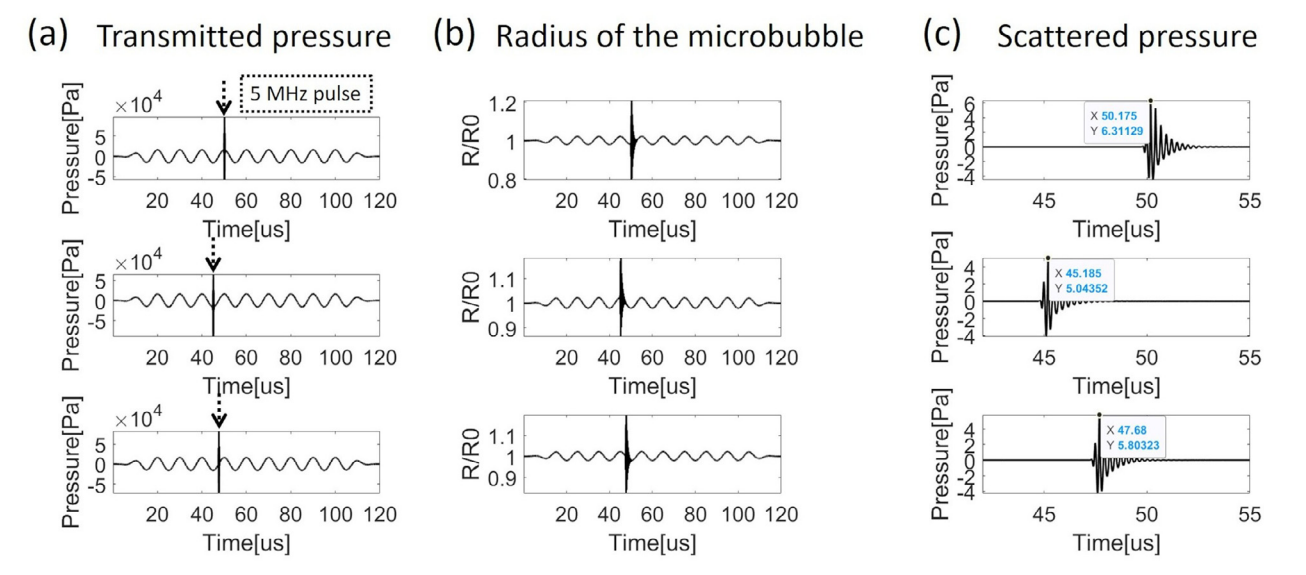


Fig. 2. Numerical simulation of dual-frequency excitation of microbubbles. (a) Dual-frequency transmitted pressure, with the *arrows* indicating the location of the 5-MHz pulse. The 5-MHz pulse was transmitted at the positive peak (top row), negative peak (middle row) and equilibrium phase (bottom row) of the 100-kHz ultrasound wave. (b) Radius of the oscillating microbubble. (c) Scattered pressure with the peak positive amplitude indicated for each condition in (a).

Figure 4a is a B-mode image of the tissue-mimicking phantom with microbubbles. Fifty frames of images were acquired for analysis. The signal of the microbubbles in the phantom channel is shown in the frequency domain (Fig. 4b). When there is no 100-kHz wave, the low-frequency component dominates the spectrum. When 100-kHz ultrasound is applied, a peak can be seen at the normalized frequency of 0.1, while another peak at the second harmonic was also seen. The signal magnitude at 0.1 was significantly higher in the presence of 100-kHz ultrasound than that without the 100-kHz ultrasound (Fig. 4c; Mann—Whitney U-test, p < 0.05). The magnitude of the signal at a normalized frequency of 0.1 increases with increasing 100-kHz acoustic pressure, although the difference is not significant.

When analyzing the amplitude of the passive cavitation detection (PCD) signal under 100 kHz excitation, the signal magnitude is not significantly higher at a pressure of 8 to 61 kPa than that without 100 kHz ultrasound (Fig. 4f). The significant increase in passive cavitation detection signal magnitude at the highest pressure level (121 kPa) indicates a significantly high frequency signal generated by the 100-kHz ultrasound alone. It should be noted that the PCD signal amplitude in Figure 4f is different from that in Figure 4c, which is the amplitude of pulse-echo signal at a normalized frequency of 0.1 in slow time. The tissue background signal is illustrated in Figure 4d and e. The tissue signal in the presence of 100-kHz ultrasound is not significantly different from that without 100-kHz ultrasound. These results indicate a

significant difference between the phantom and the microbubble in response to the low-frequency modulation.

Harmonics (200 kHz) can be detected at all pressure levels, while the ultraharmonic cavitation signal is detected only at the highest pressure (121 kPa) in the power spectrum of the signal passively received by the piston transducer (Fig. 4g). The average harmonic power at 200 kHz increased from -122 to-65 dB with the increase in 100-kHz pressure (Fig. 4h). The average ultraharmonic power (i.e., 150 kHz) at 121 kPa is -100 dB, which is significantly higher than that at lower pressure levels. There is no significant difference in the ultraharmonic power between signals obtained at 8, 16, 30 and 61 kPa and the signal obtained without 100-kHz ultrasound (Fig. 4i). It should be noted that the signal received from the piston transducer (Fig. 4g) is on a different scale than that of the PCD signal received using Verasonics (Fig. 4f).

Contrast-enhanced ultrasound imaging

In Figure 5 are F-RMI images obtained at different pressure levels. The signal magnitude of the microbubbles increases as the 100-kHz ultrasound increases, while the tissue background is mostly suppressed compared with the B-mode image in Figure 4a. At the highest pressure level, strong artifacts are visible near the phantom channel (Fig. 5f). Based on the PCD results in Figure 4f, the artifacts could be caused by the high-frequency

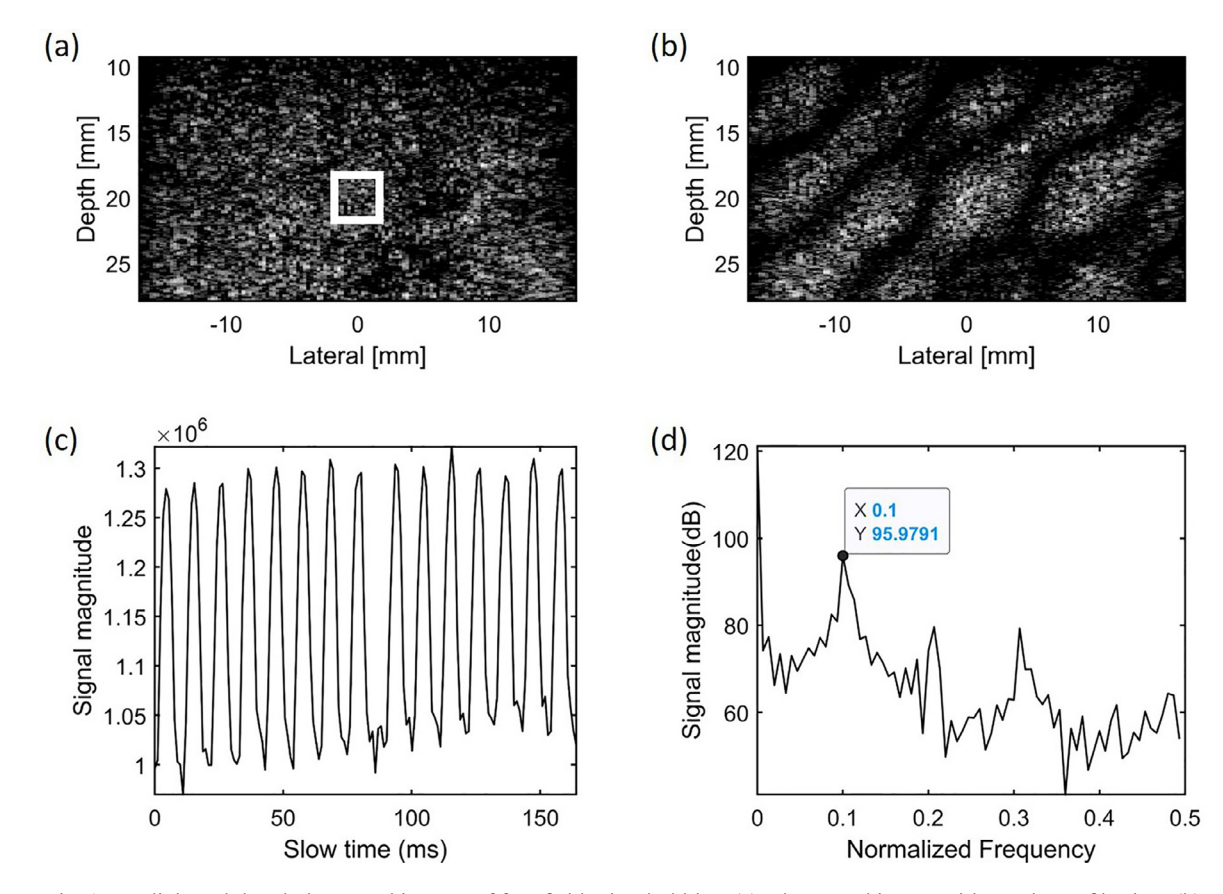


Fig. 3. Radial modulated ultrasound images of free field microbubbles. (a) Ultrasound image without clutter filtering. (b) Ultrasound image after clutter filtering in slow time. (c) Variation of signal magnitude in the slow time domain. (d) Spectrum of the signal in (c). The *white rectangle* in (a) indicates the region where the bubble signal in (c) and (d) is extracted.

signal generated by 100-kHz-modulated microbubbles and coupled to the imaging array.

Contrast-to-tissue ratio measurements of the F-RMI indicate an increase in contrast (Fig. 5g) with increasing 100-kHz acoustic pressure. The statistical test indicates that the CTR at pressure levels of 30 and 61 kPa is significantly higher than that without 100-kHz ultrasound. Overall, the frequency domain processing method produces high-contrast images of microbubbles in a stationary phantom.

Figure 6 contains S-RMI and AMPI images. The CTR of S-RMI images was higher than the CTR of F-RMI images at each pressure level (Fig. 6g). In addition, although the transmit amplitude of AMPI images was optimized before data acquisition, the CTR of AMPI images is lower than that of S-RMI images (Fig. 6g).

Imaging in the presence of tissue motion

Figure 7 includes both F-RMI and S-RMI images obtained in the presence of 1 mm/s motion. The CTR of F-RMI is approximately 0 dB (Fig. 7f), indicating failure to suppress tissue background. Applying the S-RMI

strategy with introduced motion of 1 mm/s yields CTR values up to 18 dB (Fig. 7l), although the CTRs are lower than those without tissue motion.

Images obtained in the presence of 10 mm/s motion are provided in Figure 8. The performance of the S-RMI approach (Fig. 81) still is better than that of F-RMI (Fig. 8f). The CTR when S-RMI processing is applied is approximately 10 dB in the case without 100-kHz ultrasound and the lowest pressure level (8 kPa), with the tissue background still visible after SVD filtering. The CTR of S-RMI increases when the pressure level increases from 8 to 30 kPa (Figs. 7l and 8l). However, the CTR does not increase when the pressure reaches the highest level (61 kPa). In addition, S-RMI in the presence of tissue motion provided even higher CTRs than AMPI without tissue motion.

Transcranial imaging

The average negative pressure of the continuous 100-kHz ultrasound was 18 kPa in the presence of the parietal bone and tissue-mimicking phantom. According to the free field measurement using a needle hydrophone

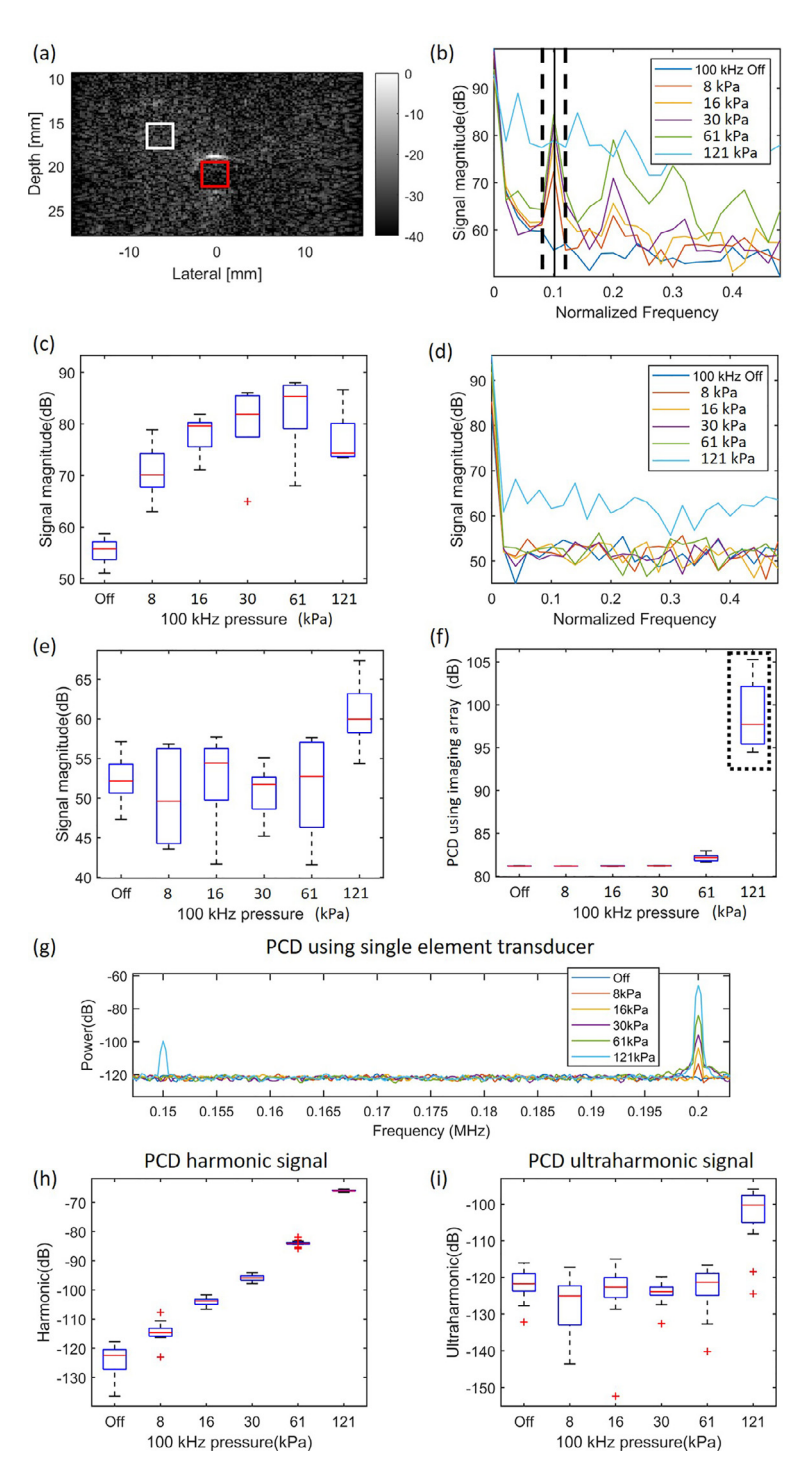


Fig. 4. Signal magnitude of radial modulation images. (a) B-Mode image of the phantom. The red rectangle indicates the region of interest in the microbubble-filled phantom channel. The white rectangle indicates the region of tissue background. (b) Signal spectrum of microbubbles in the phantom channel. (c) Signal magnitude of microbubbles at the modulation frequency (0.1) at varying driven pressures. (d) Signal spectrum of tissue background. (e) Signal magnitude of tissue background at the modulation frequency (0.1) at varying driven pressures. (f) Passive cavitation detection (PCD) signal magnitude at varying driven pressures measured using the linear imaging array. The $dashed\ rectangle$ indicates the significantly (p < 0.05) increased signal magnitudes. (g) Signal spectrum of the PCD signal acquired using the single-element transducer at varying 100-kHz pressures. (h) PCD harmonic at 0.2 MHz at varying 100-kHz pressures. (i) PCD ultraharmonic at 0.15 MHz at varying 100-kHz pressures.

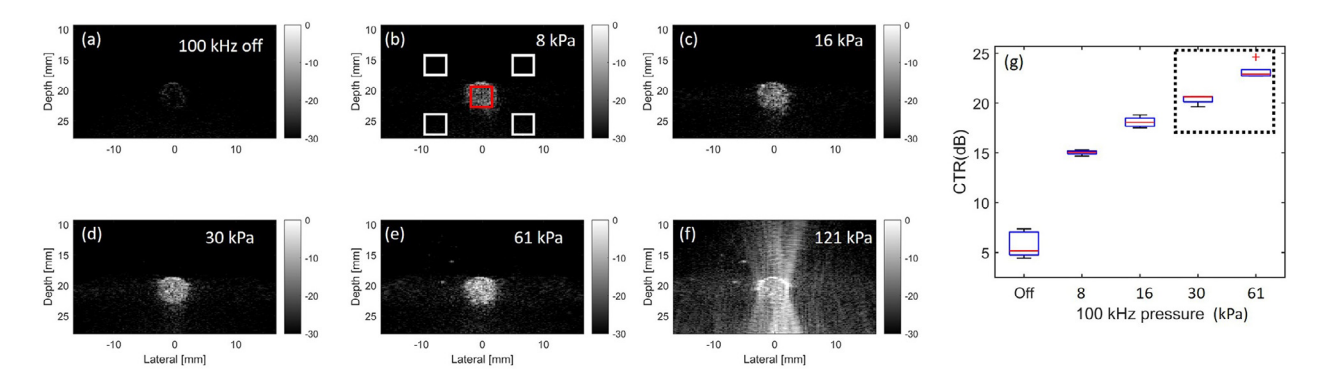


Fig. 5. Frequency domain radial modulation imaging (F-RMI) images (a-f) obtained using the frequency domain processing method at varying 100-kHz output pressure levels. (g) Contrast-to-tissue ratio (CTR) of RMI. The red *rectangle* in (b) indicates the region where the signal magnitude of microbubbles is measured. The white *rectangles* indicate the regions where the signal magnitude of tissue background is measured. The *dashed rectangle* in (g) indicates the significanly increased CTR at pressure levels of 30 and 61 kPa. The CTR is the ratio between the signal magnitudes of microbubbles and tissue background.

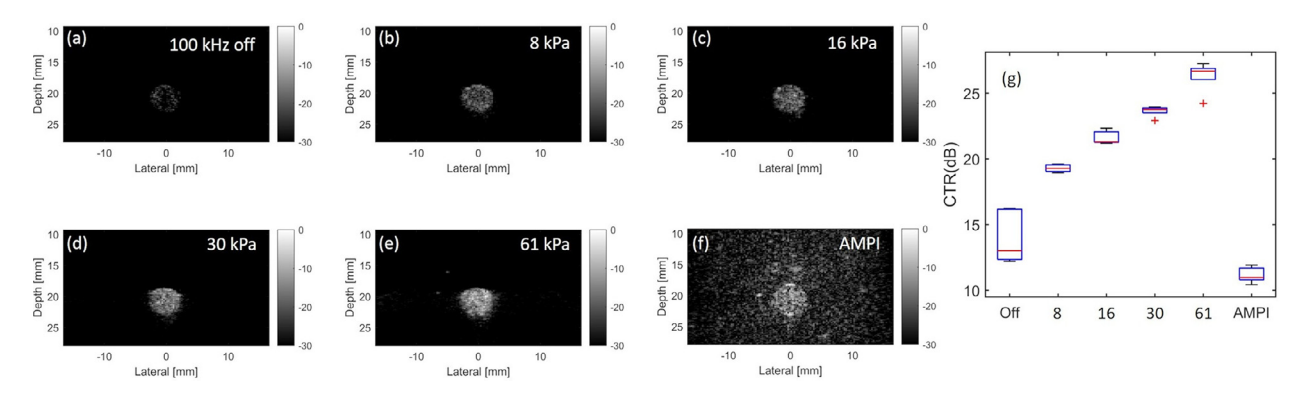


Fig. 6. Singular value decomposition-based radial modulation imaging (S-RMI) images (a—e) obtained using the singular value decomposition filter at varying 100-kHz output pressure levels. (f) Amplitude modulation pulse inversion image. (g) Contrast-to-tissue ratio (CTR) of images in (a) to (f). AMPI = amplitude modulation pulse inversion.

(HNA-0400, Onda Corp., Sunnyvale, CA, USA), the peak negative pressure of the 2-MHz imaging pulse emitted by the P4-1 array was approximately 0.23 MPa at a depth of 30 mm in the presence of a tissue-

mimicking phantom (0.4 dB/cm/MHz^{1.2}) and the 3-mm-thick temporal bone sample (attenuation: 2.8 dB/cm/MHz [White and Stevenson 1978]). In AMPI imaging, the peak negative pressure of the 1.5-MHz imaging pulse

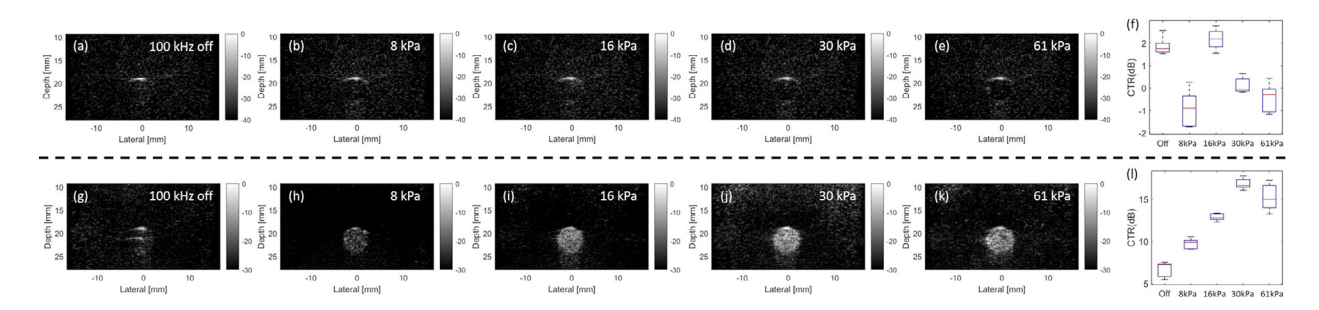


Fig. 7. Radial modulation images obtained in the presence of 1 mm/s tissue motion. (a-f) Frequency domain radial modulation imaging (F-RMI) images. (g-l) Singular value decomposition-based radial modulation imaging (S-RMI) images.

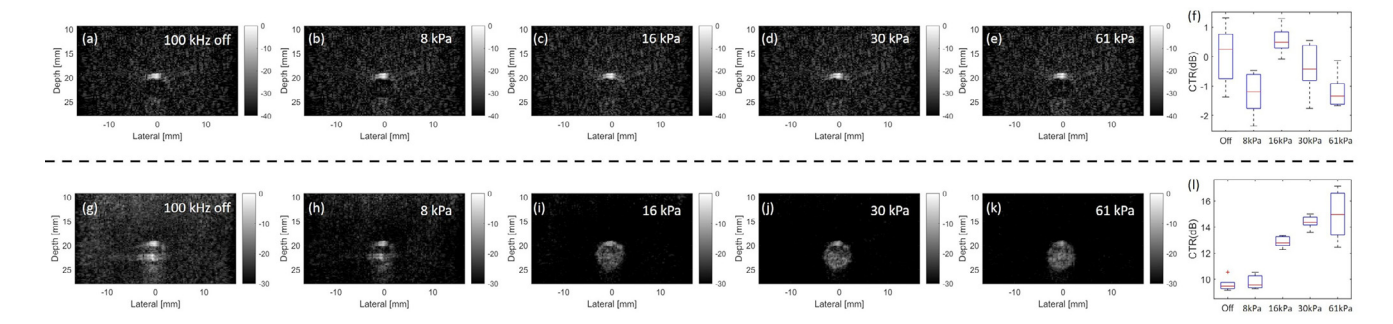


Fig. 8. Radial modulation images obtained in the presence of 10 mm/s tissue motion. (a-f) Frequency domain radial modulation imaging (F-RMI) images. (g-l) Singular value decomposition-based radial modulation imaging (S-RMI) images. CTR = contrast-to-tissue ratio

was approximately 0.17 MPa. The phantom channel filled with microbubbles was visible in the transcranial AMPI image (Fig. 9a). The measured CTR of AMPI was between 11.1 and 12.2 dB. In the S-RMI image (Fig. 9b), the tissue background, especially the signal at a depth of 5 to 25 mm, is suppressed after SVD filtering. The contrast of the phantom channel is enhanced in the S-RMI image, despite the reduced imaging resolution caused by the aberration, attenuation and reverberation in the presence of the cranial bone. The CTR values vary from 17.9 to 23.1 dB, with a mean CTR of 20.3 dB.

Effect of microbubble concentration

In this study, we also investigated the imaging performance at different microbubble concentrations. The CTR was measured at three different concentrations: 2.4×10^3 , 2.4×10^4 and 2.4×10^5 microbubbles/mL. The peak negative pressure of the 100-kHz ultrasound was 61 kPa. S-RMI images were generated via SVD filtering as described in the Methods section. As illustrated in Figure 10, there is no significant difference in CTR between concentrations of 2.4×10^3 and 2.4×10^4 . The CTR was significantly increased at the concentration of 2.4×10^5 .

DISCUSSION

As illustrated by the simulation, the variation in scattered wave amplitude indicates that 100-kHz ultrasound can modulate the echogenicity of microbubbles.

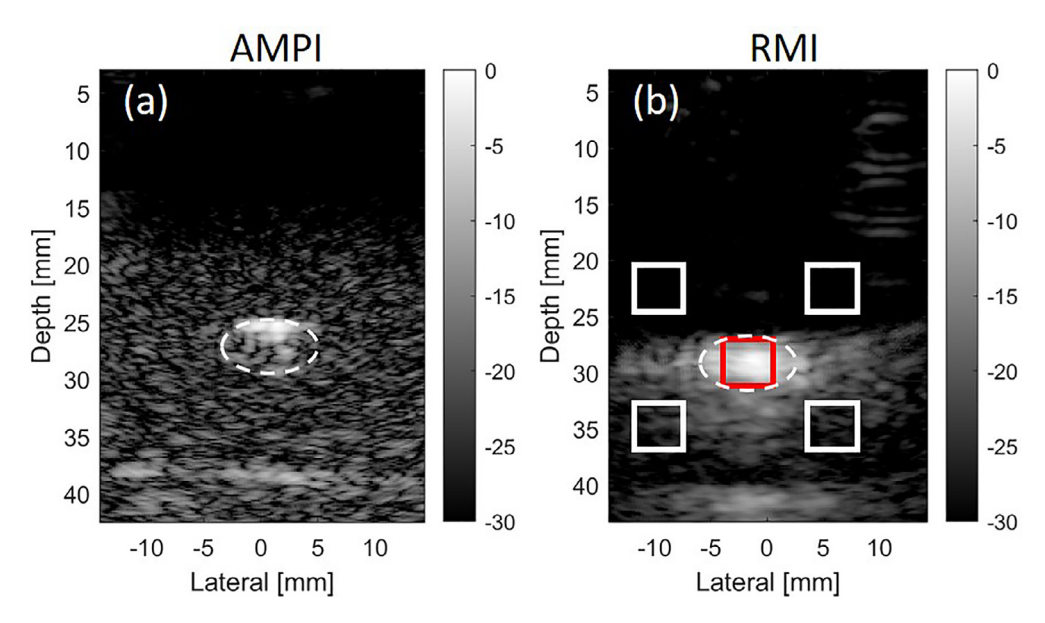


Fig 9. Transcranial imaging results. (a) Amplitude modulation pulse inversion imaging (AMPI) of microbubbles in the phantom channel. (b) Radial modulation imaging (RMI) after singular value decomposition filtering. The *red rectangle* in (b) indicates the region where the signal magnitude of microbubbles is measured. The *white rectangles* indicate the regions where the signal magnitude of tissue background is measured. The contrast-to-tissue ratio (CTR) is the ratio between the signal magnitudes of microbubbles and tissue background.

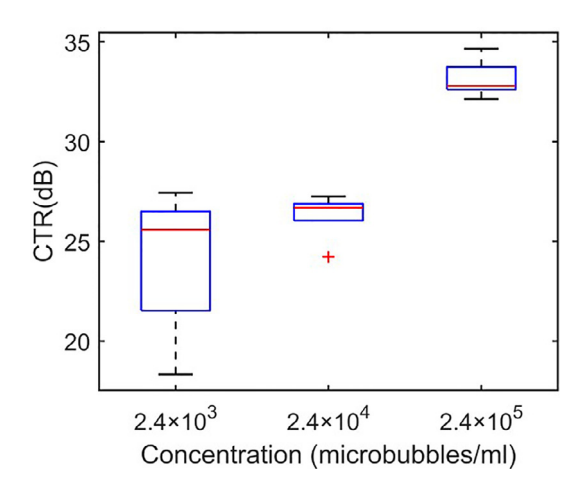


Fig. 10. Contrast-to-tissue ratio (CTR) at different microbubble concentrations.

The 100-kHz wave induced very low-amplitude, low-frequency oscillation of the microbubble (Fig. 2b), which is consistent with previous studies of microbubble oscillation at very low frequencies (Ilovitsh et al. 2018). The scattered wave amplitude at 100 kHz, which is barely discernible in Figure 2c, is much lower than the amplitude of the scattered high-frequency wave. Even with the low scattering at 100 kHz, the microbubble oscillation is sufficiently altered by this low-frequency wave to produce variation in response to the high-frequency imaging pulse, thus providing the theoretical basis for this low-frequency contrast-specific imaging approach.

The experimental results of the variation in microbubble echogenicity indicate that the modulation of microbubbles at such a low frequency is feasible even though 100 kHz is expected to be much lower than the microbubble's resonant frequency. In Figure 3b, the angled stripes can be attributed to fact that the imaging wavefront intersects with the 100-kHz modulation wavefront at a 90° angle. Low-frequency oscillation was also seen in optical images of microbubbles in previous studies using 250-kHz ultrasound transducer (Ilovitsh et al. 2018). Previously, dual-frequency acoustic cameras were used to measure the relative change in diameter of microbubbles based on modulation of the high-frequency (25–30 MHz) scattering amplitude with low-frequency ultrasound (1-5.2 MHz) near the resonant frequency; however, these frequencies are much higher than those in our study, in which microbubbles are modulated well below resonance (Renaud et al. 2012, 2014). In another study, researchers successfully used 50 kHz + 1 MHz dual-frequency ultrasound to measure the absolute diameter of bubbles at several tens of micrometers (Fouan et al. 2015). Although the absolute measurement of the changes of the diameter of the microbubbles was not assessed optically in our study, the periodic variation of the echogenicity at the modulation frequency indicates that the scattering of the imaging pulse is modulated by the low-frequency oscillation of the microbubble. Further investigation of the sensitivity of microbubbles of different sizes for the proposed low-frequency imaging technique could be performed using a high-speed camera.

As indicated by the presented RMI results, the dualfrequency transmit approach at two lower frequencies allows contrast-enhanced ultrasound imaging with deeper penetration. This could expose microbubbles to higher acoustic pressures than conventional single-frequency transmit imaging techniques because of the presence of low-frequency ultrasound. Separately, the use of very low frequency ultrasound results in an increased mechanical index and reduced pressure threshold for cavitation (Ilovitsh et al. 2018). In a recent study at 80 kHz, microbubbles are destroyed at peak negative pressures of 120 kPa (Bismuth et al. 2021). Alternatively, at 120 kHz, the broadband signal indicates the occurrence of microbubble inertial cavitation at approximately 100 kPa (Gruber et al. 2014). These reports indicate that low-frequency ultrasound could cause microbubble destruction even at low pressures. For diagnostic imaging, inertial cavitation and potentially accompanying irreversible bio-effects should be avoided (Ter Haar 2002, 2009). In our study, the mechanical index at 100 kHz was 0.025, 0.05, 0.09 and 0.19 at pressures of 8, 16, 30 and 61 kPa, respectively. The mechanical index was below 0.3, which is the safety threshold recommended in the previous study (Fouan et al. 2015). However, further study is required to investigate these safety considerations, as stable cavitation of microbubbles may only be possible within a narrow range of low acoustic pressures at low frequencies (<1 MHz).

In our study, a single-element piston transducer (V309) was also used as a passive receiver to monitor the signal (harmonics and ultraharmonics) arising from microbubbles excited by the 100-kHz ultrasound. The ultraharmonics detected at 121 kPa (Fig. 4i) indicate that the threshold pressure of ultraharmonics is between 61 and 121 kPa, which is similar to the results from the previous study (Gruber et al. 2014). In this previous study, Gruber et al. found that the ultraharmonic threshold for Definity microbubbles at 120 kHz is approximately 100 kPa (200 kPa peak-to-peak pressure). These results also indicate that the high-contrast images (Fig. 5) without artifacts were obtained below the threshold of ultraharmonics at 100 kHz.

Tissue motion is ubiquitous and arises from respiration, cardiac pulsation and movement of the transducer. Thus, the microbubbles in capillaries are expected to move with the tissue in the field of view during imaging. The F-RMI processing technique (Fig. 5) produced high-contrast images of microbubbles in a stationary phantom. However, the F-RMI results obtained in the presence of simulated tissue motion indicate the frequency domain processing method is not capable of separating the microbubbles from surrounding tissue (Figs. 7 and 8). The comparison indicates that the S-RMI processing technique outperforms F-RMI in tissue signal suppression and contrast enhancement.

In the presence of tissue motion, the contrast of S-RMI (Figs. 7 and 8) increases with increasing 100-kHz pressure until 30 kPa. There is no significant improvement in the CTR when the pressure is increased to 61 kPa, possibly because the variation in spatiotemporal coherence induced by tissue motion reduces the benefit from the further increase in low-frequency ultrasound pressure. In this study, tissue motion was simulated only along the axial direction. Nevertheless, given that SVD filtering operates on differences in spatial coherence between microbubbles and tissue, the contrast enhancement of S-RMI is still expected to be valid for *in vivo* imaging, when tissue motion could be more complex and larger in magnitude relative to the constant axial motion simulated in this study (Desailly et al. 2017).

The reason why we used only 50 frames is to maintain a final frame rate of approximately 20 frames/s (~1000/50) for real-time imaging as described in the Methods section. In addition, unlike the less echogenic red blood cells in Huang et al. (2021), the echogenicity of the microbubble already provides sufficient SNR to enable separation of contrast agents and tissue background. However, it should also be noted that the image contrast and sensitivity could be further increased by increasing the number of frames used in SVD filtering (at the expense of decreased frame rate), as the separation of tissue, microbubbles and noise is easier with more frames.

The selection of the cutoff value of the SVD filter affects image contrast; however, the cutoff value is not predetermined or automatically computed for S-RMI (Figs. 7 and 8) with tissue motion. As shown in a previous study of ultrafast Doppler imaging, the selection of optimal cutoff value is affected by the spatial—temporal statistics of the tissue and blood/microbubble signals (Demené et al. 2015). In this study, the presence of the low-frequency ultrasound is an additional factor that changes the spatiotemporal statistics of the signal. Development of an automated method for estimation of the optimal cutoff value is needed based on data acquired in different *in vivo* imaging scenarios.

In this study, the main purpose was to develop strategies for imaging targeted microbubbles (molecular imaging) or the slowest flowing microbubbles. Therefore, the effect of flow was not quantified in this study.

However, it should be noted that the performance of F-RMI is expected to be affected by the flow because the spectrum of the slow-time signal will be altered by the flow. On the other hand, the performance of S-RMI could be enhanced in the presence of flow because of the capability of the SVD filter to separate the microbubbles from the tissue based on the spatial—temporal statistical coherence.

Results in a transcranial imaging phantom (Fig. 9) indicate it is feasible to use a 100 kHz + 2 MHz transmit strategy for transcranial imaging through the highly attenuating cranial bone. Even with reduced microbubble modulation far below resonance, 100-kHz low-frequency ultrasound not only provides sufficient penetration through the skull but also enables sufficient separation between the modulation frequency and imaging frequency so that high-CTR images can be obtained. However, there is a sharp increase in signal magnitude at the depth in the phantom where the channel is located and additional echogenic regions near the channel (Fig. 9b). These signals outside the phantom channel appear to be correlated with the signal in the phantom channel, which indicates that these signals may be attributed to the sidelobes arising from the single-angle plane wave transmit events or the aberration and the multiple reflections of bubble signals induced by the cranial bone. Moreover, in this study, transcranial imaging was tested using 2-MHz imaging pulses. Penetration depth would be increased by further reducing the imaging frequency to 1 MHz or lower as long as the higher-order harmonics induced by 100-kHz ultrasound are not coupled to the imaging bandwidth. The further decrease in imaging frequency could benefit high-contrast transcranial imaging through the thick cranial bone beyond the temporal bone window (Lindsey et al. 2013).

A limitation of this study is that the 100-kHz transducer was placed perpendicular to the imaging array, which is likely not feasible for in vivo imaging. However, in the transcranial imaging experiment, imaging was demonstrated with the 100-kHz transducer positioned to transmit through a thicker, more attenuating part of the skull, which is a realistic representation of the required in vivo imaging scenario with two transducers. In addition, unlike previous dual-frequency ultrasound transducers (Bouakaz et al. 2002a; Gessner et al. 2010; Guiroy et al. 2013; Li et al. 2018; Lindsey et al. 2017a), the 100-kHz ultrasound used in the presented approach, RMI, is much lower in frequency. Additional optimization of the radiation beam profile would be needed given the near-field perturbation of pressure and safety concerns related to the inertial cavitation threshold at such a low frequency.

Moreover, compared with the previous study of ultrafast radial modulation imaging techniques (Muleki-

Seya et al. 2019), the low-frequency (100 kHz) radial modulation imaging technique offers several advantages. First, the ultrasound frequency used to modulate and detect microbubbles is significantly lower, which enables high-contrast imaging for clinical scenarios involving deep targets and unfavorable imaging windows in some patients, such as the liver and brain. Furthermore, because the frame rate of the presented RMI technique is no longer constrained by the number of oscillation states of modulated microbubbles, an increased number of imaging transmit events at a lower PRF can be used for imaging targets with increased depth. Real-time (~20 frames/s) contrast-enhanced imaging is achievable by using short ensembles (i.e., 50 frames). Finally, highcontrast imaging in the presence of tissue motion has been determined to be feasible by using singular value decomposition filtering.

CONCLUSIONS

The feasibility of modulating microbubble echogenicity using very low frequency (100 kHz) ultrasound has been determined. This very low frequency radial modulation imaging strategy could be used for real-time, high-penetration-depth contrast-enhanced ultrasound imaging, especially in the presence of tissue motion. In addition, this imaging strategy could be used in transcranial imaging. The novel contrast-enhanced ultrasound imaging strategy developed could also be beneficial in abdominal applications such as liver perfusion imaging, in which high penetration depth is required and image quality can be highly patient specific.

Acknowledgments—This work was supported by National Science Foundation CMMI Award No. 1933158 on Coupling Skull—Brain Vibroacoustics and Ultrasound toward Enhanced Imaging, Diagnosis, and Therapy. The authors thank M. Sait Kilinc, Dr. F. Levent Degertekin, Pradosh P. Dash, Hohyun Lee, Ahmed Allam, Dr. Costas D. Arvanitis and Dr. Alper Erturk for helpful discussions and help with acoustic calibration of the 100-kHz transducer.

Conflict of interest disclosure—The authors have no relevant conflicts of interest to disclose.

REFERENCES

- American Institute of Ultrasound in Medicine (AIUM). AIUM practice guideline for the performance of an ultrasound examination of the abdomen and/or retroperitoneum. J Ultrasound Med 2012;31:1301–1312.
- Averkiou M, Lampaskis M, Kyriakopoulou K, Skarlos D, Klouvas G, Strouthos C, Leen E. Quantification of tumor microvascularity with respiratory gated contrast enhanced ultrasound for monitoring therapy. Ultrasound Med Biol 2010;36:68–77.
- Averkiou MA, Bruce MF, Powers JE, Sheeran PS, Burns PN. Imaging methods for ultrasound contrast agents. Ultrasound Med Biol 2020;46:498–517.
- Bismuth M, Katz S, Rosenblatt H, Twito M, Aronovich R, Ilovitsh T. Acoustically detonated microbubbles coupled with low frequency insonation: Multiparameter evaluation of low energy mechanical ablation. Bioconjug Chem 2021;, doi: 10.1021/acs.bioconjchem.1c00203 In press. Available at.

- Bouakaz A, Frigstad S, Ten Cate FJ, de Jong N. Improved contrast to tissue ratio at higher harmonics. Ultrasonics 2002a;40:575–578.
- Bouakaz A, Frigstad S, Ten Cate FJ, de Jong N. Super harmonic imaging: A new imaging technique for improved contrast detection. Ultrasound Med Biol 2002b;28:59–68.
- Bouakaz A, Krenning BJ, Vletter WB, Ten Cate FJ, De Jong N. Contrast superharmonic imaging: A feasibility study. Ultrasound Med Biol 2003;29:547–553.
- Bouakaz A, Versluis M, Borsboom J, De Jong N. Radial modulation of microbubbles for ultrasound contrast imaging. IEEE Trans Ultrason Ferroelectr Freq Control 2007;54:2283–2290.
- Cheng CH, Shen CC, Yeh CK. Dual-frequency chirp imaging for contrast detection. Phys Med Biol 2011;56:2767–2778.
- Chérin E, Brown J, Måsøy S-E, Shariff H, Karshafian R, Williams R, Burns PN, Foster FS. Radial modulation imaging of microbubble contrast agents at high frequency. Ultrasound Med Biol 2008;34:949–962.
- Couture O, Aubry JF, Montaldo G, Tanter M, Fink M. Suppression of tissue harmonics for pulse-inversion contrast imaging using time reversal. Phys Med Biol 2008;53:5469–5480.
- Demené C, Deffieux T, Pernot M, Osmanski BF, Biran V, Gennisson JL, Sieu LA, Bergel A, Franqui S, Correas JM. Spatiotemporal clutter filtering of ultrafast ultrasound data highly increases Doppler and fUltrasound sensitivity. IEEE Trans Med Imaging 2015;34:2271–2285.
- Desailly Y, Tissier AM, Correas JM, Wintzenrieth F, Tanter M, Couture O. Contrast enhanced ultrasound by real-time spatiotemporal filtering of ultrafast images. Phys Med Biol 2017;62:31–42.
- Dietrich CF, Averkiou MA, Correas JM, Lassau N, Leen E, Piscaglia F. An EFSUMB introduction into dynamic contrast-enhanced ultrasound (DCE-US) for quantification of tumour perfusion. Ultraschall Med 2012;33:344–351.
- Eckersley RJ, Chin CT, Burns PN. Optimising phase and amplitude modulation schemes for imaging microbubble contrast agents at low acoustic power. Ultrasound Med Biol 2005;31:213–219.
- Eisenbrey JR, Dave JK, Halldorsdottir VG, Merton DA, Machado P, Liu JB, Miller C, Gonzalez JM, Park S, Dianis S, Chalek CL, Thomenius KE, Brown DB, Navarro V, Forsberg F. Simultaneous grayscale and subharmonic ultrasound imaging on a modified commercial scanner. Ultrasonics 2011;51:890–897.
- Emmer M, Vos HJ, Versluis M, De Jong N. Radial modulation of single microbubbles. IEEE Trans Ultrason Ferroelectr Freq Control 2009;56:2370–2379.
- Erlichman DB, Weiss A, Koenigsberg M, Stein MW. Contrast enhanced ultrasound: A review of radiology applications. Clin Imaging 2020;60:209–215.
- Errico C, Pierre J, Pezet S, Desailly Y, Lenkei Z, Couture O, Tanter M. Ultrafast ultrasound localization microscopy for deep super-resolution vascular imaging. Nature 2015;527:499–502.
- Forsberg F, Liu JB, Shi WT, Ro R, Lipcan KJ, Deng XD, Hall AL. In vivo perfusion estimation using subharmonic contrast microbubble signals. J Ultrasound Med 2006;25:15–21.
- Fouan D, Achaoui Y, Payan C, Mensah S. Microbubble dynamics monitoring using a dual modulation method. J Acoust Soc Am 2015:137:EL144–EL150.
- Gessner R, Lukacs M, Lee M, Cherin E, Foster FS, Dayton PA. High-resolution, high-contrast ultrasound imaging using a prototype dual-frequency transducer: In vitro and in vivo studies. IEEE Trans Ultrason Ferroelectr Freq Control 2010;57:1772–1781.
- Gong P, Song P, Chen S. Improved contrast-enhanced ultrasound imaging with multiplane-wave imaging. IEEE Trans Ultrason Ferroelectr Freq Control 2018;65:178–187.
- Gruber MJ, Bader KB, Holland CK. Cavitation thresholds of contrast agents in an in vitro human clot model exposed to 120-kHz ultrasound. J Acoust Soc Am 2014;135:646-653.
- Guiroy A, Novell A, Ringgaard E, Lou-Moeller R, Gregoire JM, Abellard AP, Zawada T, Bouakaz A, Levassort F. Dual-frequency transducer for nonlinear contrast agent imaging. IEEE Trans Ultrason Ferroelectr Freq Control 2013;60:2634–2644.
- Hansen R, Angelsen BA. SURF imaging for contrast agent detection. IEEE Trans Ultrason Ferroelectr Freq Control 2009;56:280–290.

- Huang C, Song P, Trzasko JD, Gong P, Lok UW, Tang S, Manduca A, Chen S. Simultaneous noise suppression and incoherent artifact reduction in ultrafast ultrasound vascular imaging. IEEE Trans Ultrason Ferroelectr Freq Control 2021;68:2075–2085.
- Ilovitsh T, Ilovitsh A, Foiret J, Caskey CF, Kusunose J, Fite BZ, Zhang H, Mahakian LM, Tam S, Butts-Pauly K. Enhanced microbubble contrast agent oscillation following 250 kHz insonation. Sci Rep 2018;8:1–15.
- Jang HJ, Yu HJ, Kim TK. Contrast-enhanced ultrasound in the detection and characterization of liver tumors. Cancer Imaging 2009:9:96-103
- Jing B, Brown ME, Davis ME, Lindsey BD. Imaging the activation of low-boiling-point phase-change contrast agents in the presence of tissue motion using ultrafast inter-frame activation ultrasound imaging. Ultrasound Med Biol 2020a;46:1474–1489.
- Jing B, Kashyap EP, Lindsey BD. Transcranial activation and imaging of low boiling point phase-change contrast agents through the temporal bone using an ultrafast interframe activation ultrasound sequence. Med Phys 2020b;47:4450–4464.
- Kern R, Diels A, Pettenpohl J, Kablau M, Brade J, Hennerici MG, Meairs S. Real-time ultrasound brain perfusion imaging with analysis of microbubble replenishment in acute MCA stroke. J Cereb Blood Flow Metab 2011;31:1716–1724.
- Krishnan S, Hamilton JD, O'Donnell M. Suppression of propagating second harmonic in ultrasound contrast imaging. IEEE Trans Ultrason Ferroelectr Freq Control 1998;45:704–711.
- Kruse DE, Ferrara KW. A new imaging strategy using wideband transient response of ultrasound contrast agents. IEEE Trans Ultrason Ferroelectr Freq Control 2005;52:1320–1329.
- Kusunose J, Caskey CF. Fast, low-frequency plane-wave imaging for ultrasound contrast imaging. Ultrasound Med Biol 2018;44:2131– 2142
- Li S, Kim J, Wang Z, Kasoji S, Lindsey BD, Dayton PA, Jiang X. A dual-frequency colinear array for acoustic angiography in prostate cancer evaluation. IEEE Trans Ultrason Ferroelectr Freq Control 2018;65:2418–2428.
- Lin FL, Shelton SE, Espindola D, Rojas JD, Pinton G, Dayton PA. 3-D ultrasound localization microscopy for identifying microvascular morphology features of tumor angiogenesis at a resolution beyond the diffraction limit of conventional ultrasound. Theranostics 2017;7:196–204.
- Lindsey BD, Nicoletto HA, Bennett ER, Laskowitz DT, Smith SW. Simultaneous bilateral real-time 3-D transcranial ultrasound imaging at 1 MHz through poor acoustic windows. Ultrasound Med Biol 2013;39:721–734.
- Lindsey BD, Nicoletto HA, Bennett ER, Laskowitz DT, Smith SW. 3-D transcranial ultrasound imaging with bilateral phase aberration correction of multiple isoplanatic patches: A pilot human study with microbubble contrast enhancement. Ultrasound Med Biol 2014a;40:90–101.
- Lindsey BD, Rojas JD, Martin KH, Shelton SE, Dayton PA. Acoustic characterization of contrast-to-tissue ratio and axial resolution for dual-frequency contrast-specific acoustic angiography imaging. IEEE Trans Ultrason Ferroelectr Freq Control 2014b;61:1668– 1687
- Lindsey BD, Rojas JD, Dayton PA. On the relationship between microbubble fragmentation, deflation and broadband superharmonic signal production. Ultrasound Med Biol 2015;41:1711–1725.
- Lindsey BD, Kim J, Dayton PA, Jiang X. Dual-frequency piezoelectric endoscopic transducer for imaging vascular invasion in pancreatic cancer. IEEE Trans Ultrason Ferroelectr Freq Control 2017a;64:1078–1086.
- Lindsey BD, Shelton SE, Martin KH, Ozgun KA, Rojas JD, Foster FS, Dayton PA. High resolution ultrasound superharmonic perfusion imaging: In vivo feasibility and quantification of dynamic contrastenhanced acoustic angiography. Ann Biomed Eng 2017b;45:939– 948
- Lyshchik A, Kono Y, Dietrich CF, Jang HJ, Kim TK, Piscaglia F, Vezeridis A, Willmann JK, Wilson SR. Contrast-enhanced ultrasound of the liver: technical and lexicon recommendations from

- the ACR CEUS LI-RADS working group. Abdom Radiol 2018;43:861–879.
- Masoy SE, Standal O, Nasholm P, Johansen TF, Angelsen B, Hansen R. SURF imaging: In vivo demonstration of an ultrasound contrast agent detection technique. IEEE Trans Ultrason Ferroelectr Freq Control 2008;55:1112–1121.
- Morgan KE, Allen JS, Dayton PA, Chomas JE, Klibaov AL, Ferrara KW. Experimental and theoretical evaluation of microbubble behavior: Effect of transmitted phase and bubble size. IEEE Trans Ultrason Ferroelectr Freq Control 2000;47:1494–1509.
- Mule S, Kachenoura N, Lucidarme O, De Oliveira A, Pellot-Barakat C, Herment A, Frouin F. An automatic respiratory gating method for the improvement of microcirculation evaluation: Application to contrast-enhanced ultrasound studies of focal liver lesions. Phys Med Biol 2011;56:5153–5165.
- Muleki-Seya P, Xu K, Tanter M, Couture O. Ultrafast radial modulation imaging. IEEE Trans Ultrason Ferroelectr Freq Control 2019;67:598–611.
- Phillips P. Contrast pulse sequences (CPS): Imaging nonlinear microbubbles. Proc IEEE Int Ultrason Symp 2001;1739–1745.
- Phillips LC, Klibanov AL, Wamhoff BR, Hossack J. Intravascular ultrasound mediated delivery of DNA via microbubble carriers to an injured porcine artery in vivo. Proc IEEE Int Ultrason Symp 2008;1154–1157.
- Putz FJ, Verloh N, Erlmeier A, Schelker RC, Schreyer AG, Hautmann MG, Stroszczynski C, Banas B, Jung EM. Influence of limited examination conditions on contrast-enhanced sonography for characterising liver lesions. Clin Hemorheol Microcirc 2019;71:267–276.
- Renaud G, Bosch J, Van der Steen A, de Jong N. An "acoustical camera" for in vitro characterization of contrast agent microbubble vibrations. Appl Phys Lett 2012;100 101911.
- Renaud G, Bosch JG, Van Der Steen AF, De Jong N. Low-amplitude non-linear volume vibrations of single microbubbles measured with an "acoustical camera. Ultrasound Med Biol 2014;40:1282–1295
- Seidel G, Albers T, Meyer K, Wiesmann M. Perfusion harmonic imaging in acute middle cerebral artery infarction. Ultrasound Med Biol 2003:29:1245–1251
- Seidel G, Roessler F, Al-Khaled M. Microvascular imaging in acute ischemic stroke. J Neuroimaging 2013;23:166–169.
- Seppenwoolde Y, Shirato H, Kitamura K, Shimizu S, van Herk M, Lebesque JV, Miyasaka K. Precise and real-time measurement of 3D tumor motion in lung due to breathing and heartbeat, measured during radiotherapy. Int J Radiat Oncol Biol Phys 2002;53:822–
- Shariff HH, Bevan PD, Karshafian R, Williams R, Burns PN. Radial modulation imaging: Raising the frequency for contrast imaging. Proc IEEE Int Ultrason Symp 2006;104–107.
- Shelton SE, Lindsey BD, Tsuruta JK, Foster FS, Dayton PA. Molecular acoustic angiography: A new technique for high-resolution superharmonic ultrasound molecular imaging. Ultrasound Med Biol 2016;42:769–781.
- Shen CC, Yan JH. High-order Hadamard-encoded transmission for tissue background suppression in ultrasound contrast imaging: Memory effect and decoding schemes. IEEE Trans Ultrason Ferroelectr Freq Control 2019;66:26–37.
- Shi WT, Forsberg F, Hall AL, Chiao RY, Liu JB, Miller S, Thomenius KE, Wheatley MA, Goldberg BB. Subharmonic imaging with microbubble contrast agents: Initial results. Ultrason Imaging 1999;21:79–94.
- Sidhu PS, Cantisani V, Dietrich CF, Gilja OH, Saftoiu A, Bartels E, Bertolotto M, Calliada F, Clevert DA, Cosgrove D, Deganello A, D'Onofrio M, Drudi FM, Freeman S, Harvey C, Jenssen C, Jung EM, Klauser AS, Lassau N, Meloni MF, Leen E, Nicolau C, Nolsoe C, Piscaglia F, Prada F, Prosch H, Radzina M, Savelli L, Weskott HP, Wijkstra H. The EFSUMB guidelines and recommendations for the clinical practice of contrast-enhanced ultrasound (CEUS) in non-hepatic applications: Update 2017 (long version). Ultraschall Med 2018;39:E2–E44.

- Stanziola A, Toulemonde M, Li Y, Papadopoulou V, Corbett R, Duncan N, Eckersley RJ, Tang MX. Motion artifacts and correction in multipulse high-frame rate contrast-enhanced ultrasound. IEEE Trans Ultrason Ferroelectr Freq Control 2019;66:417–420.
- Strobel D, Seitz K, Blank W, Schuler A, Dietrich C, von Herbay A, Friedrich-Rust M, Kunze G, Becker D, Will U, Kratzer W, Albert FW, Pachmann C, Dirks K, Strunk H, Greis C, Bernatik T. Contrast-enhanced ultrasound for the characterization of focal liver lesions— Diagnostic accuracy in clinical practice (DEGUM multicenter trial). Ultraschall Med 2008;29:499–505.
- Tang MX, Kamiyama N, Eckersley RJ. Effects of nonlinear propagation in ultrasound contrast agent imaging. Ultrasound Med Biol 2010;36:459–466.
- Ter Haar G. Ultrasonic contrast agents: safety considerations reviewed. Eur J Radiol 2002;41:217–221.
- Ter Haar G. Safety and bio-effects of ultrasound contrast agents. Med Biol Eng Comput 2009;47:893–900.
- Tu J, Swalwell JE, Giraud D, Cui WC, Chen WZ, Matula TJ. Microbubble sizing and shell characterization using flow cytometry. IEEE Trans Ultrason Ferroelectr Freq Control 2011;58:955–963.
- Vinke EJ, Kortenbout AJ, Eyding J, Slump CH, van der Hoeven JG, de Korte CL, Hoedemaekers CWE. Potential of contrast-enhanced

- ultrasound as a bedside monitoring technique in cerebral perfusion: A systematic review. Ultrasound Med Biol 2017;43:2751–2757.
- Wang D, Cloutier G, Fan Y, Hou Y, Su Z, Su Q, Wan M. Automatic respiratory gating hepatic DCEUS-based dual-phase multiparametric functional perfusion imaging using a derivative principal component analysis. Theranostics 2019;9:6143.White DN, Stevenson RJ. The acoustic characteristics of the skull.
- White DN, Stevenson RJ. The acoustic characteristics of the skull. Ultrasound Med Biol 1978;4:225–252.
- Whittingham TA, Quaia E. Contrast-specific imaging techniques: technical perspective. Heidelberg/Berlin: Springer; 2005. p. 43–70 Contrast media in ultrasonography.
- Wu W, Chen MH, Yin SS, Yan K, Fan ZH, Yang W, Dai Y, Huo L, Li JY. The role of contrast-enhanced sonography of focal liver lesions before percutaneous biopsy. AJR Am J Roentgenol 2006;187:752–761.
- Yoon SH, Lee KH, Kim SY, Kim YH, Kim JH, Lee SH, Kim TK. Real-time contrast-enhanced ultrasound-guided biopsy of focal hepatic lesions not localised on B-mode ultrasound. Eur Radiol 2010;20:2047–2056.
- Yu FTH, Villanueva FS, Chen X. Radial modulation contrast imaging using a 20-MHz single-element intravascular ultrasound catheter. IEEE Trans Ultrason Ferroelectr Freq Control 2014;61:779–791.
- Zhao S, Kruse D, Ferrara K, Dayton P. Selective imaging of adherent targeted ultrasound contrast agents. Phys Med Biol 2007;52:2055.